Received 6 September 2016; revised 24 October 2016; accepted 30 October 2016. Date of publication 2 November 2016;
date of current version 20 December 2016. The review of this paper was arranged by Editor C. C. McAndrew.

Digital Object Identifier 10.1109/JEDS.2016.2623799

CMOS Image Sensor Random Telegraph Noise Time Constant Extraction From Correlated To Uncorrelated Double Sampling

CALVIN YI-PING CHAO, (Member, IEEE), HONYIH TU, THOMAS WU, KUO-YU CHOU, SHANG-FU YEH, (Member, IEEE), AND FU-LUNG HSUEH, (Life Member, IEEE)

Taiwan Semiconductor Manufacturing Company, Hsinchu 300-77, Taiwan

CORRESPONDING AUTHOR: C. Y.-P. CHAO (e-mail: calvin_chao@tsmc.com)

ABSTRACT A new method for on-chip random telegraph noise (RTN) characteristic time constant extraction using the double sampling circuit in an 8.3 Mpixel CMOS image sensor is described. The dependence of the measured RTN on the time difference between the double sampling and the key equation used for time constant extraction are derived from the continuous time RTN model and the discrete event RTN model. Both approaches lead to the same result and describe the data reasonably well. From the detailed study of the noisiest 1000 pixels, we find that about 75% to 85% of them show the signature of a single-trap RTN behavior with three distinct signal levels, and about 96% of the characteristic time constants fall between 1 μs and 500 μs with the median around 10 μs at room temperature.

INDEX TERMS Random telegraph noise (RTN), CMOS image sensor (CIS), correlated double sampling (CDS).

I. INTRODUCTION

The random telegraph noise (RTN) in small semiconductor devices [1]–[7] has adverse impact on the performance of a broad range of products such as the DRAM [8], [9], the SRAM [10], [11], the Flash memories [12], [13], the digital circuits [14], [15], as well as the CMOS image sensors (CIS) [16]–[35]. The RTN is called the circuit designer's nightmare [6] partly because it is difficult to be modeled for and used in circuit simulation either in the time domain or in the frequency domain. The RTN typically shows a highly skewed non-Gaussian distribution with a wide range of time constant, making it difficult to specify the worst-case process corners. For the array type of devices such as the memories and imager sensors, the percentage of cells showing clear RTN behavior may not be high, but the impact on the yield, the error rates, and the image quality cannot be ignored.

The sources of the RTN are generally believed to be the charge traps related to the defects inside the gate oxide and at the oxide-silicon interface. To fully understand the RTN, it is necessary to characterize the statistical noise distribution, the emission-capture time constants, the activation energies, the power density spectra, the physical sources, locations, and the relations to fabrication process details. In this paper, we focus on the characteristic time constants. While most of the RTN time constant extractions reported in the literature [1], [2], [28]–[35] were based on the telegraphic waveforms of measured voltages or currents, we developed a new method of on-chip time constant extraction for the CIS with double sampling circuits. From the noise dependence on the time difference between the double sampling, the time constants for a large number of pixels can be extracted simultaneously.

The test chip is described in Section II. The RTN distributions are summarized in Section III. The theoretical equation underlying the time constant extraction method is derived from both the continuous-time model in Section IV and the discrete-event model in Section V, respectively. The pixel by pixel extraction results are discussed in Section VI. The conclusion is given in Section VII.

II. THE 8.3 MPIXEL CIS TEST CHIP

The data presented in this article are measured from an 8.3 Mpixel CIS test chip using a N45 Backside Illuminated (BSI) CIS technology, with a 2-by-2 shared,

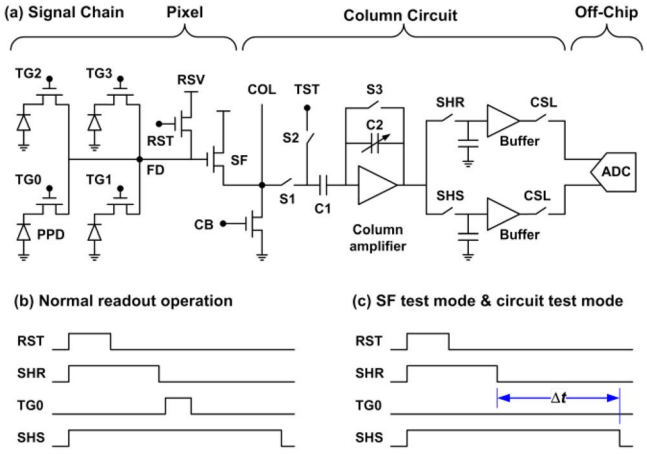

FIGURE 1. **(a) The simplified signal chain schematic; (b) the timing diagram for the normal readout operation; (c) the test mode timing diagram with a programmable time difference Δt from 0 to 25 μs.**

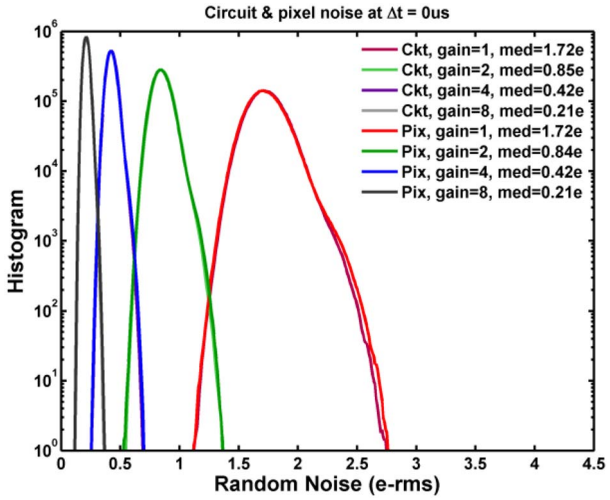

FIGURE 2. **The readout circuit-only noises and the pixel SF plus circuit noises at various gains measured using the test mode with Δt set to 0. The pixel plus circuit noise curves almost overlap with the circuit-only noise curves, indicating that the SF noises are cancelled by CDS in this case.**

1.1-μm pixel structure and an average of 1.5 transistors per pixel cell. Fig. 1(a) shows the simplified signal chain schematic. The column circuit consists of a switched-capacitor amplifier with a programmable gain from 1X to 8X, the sample-and-hold circuits, the buffers for the correlated double sampling (CDS), and the column-select (CSL) switches. The differential CDS output is digitized by an off-chip 14-bit ADC with a 2-V differential input range, clocked at 10 MHz.

The pinned photodiode (PPD) in each pixel has an average full-well capacity (FWC) around 6,000 e-. The source-follower (SF) is a Vt-tailored NMOS with W = 0.2 μm and L = 0.8 μm. The average SF gain is 0.85 when biased at a 4 μA constant current. The measured system conversion factors by the photon transfer curve (PTC) method [36] are 1.24 e-/DN, 0.61 e-/DN, 0.315 e-/DN, and 0.153 e-/DN at 1X, 2X, 4X, and 8X gain, respectively. The estimated pixel floating diffusion (FD) capacitance is 1.34 fF and the corresponding conversion gain is 120 μV/e-.

The even- and odd-column pixels are read out alternatively in the first and the second half-line time. Fig. 1(b) shows the timing diagram for the normal readout operation with 4 sequential steps: (1) the floating diffusion reset (RST), (2) the sample-and-hold of the reset voltage (SHR), (3) the charge transfer (TG0), and (4) the sample-and-hold of the signal voltage (SHS).

In this study we are concerned with the device and process related noises. As such, all the data are measured in the dark so that the photo signals and the photon shot noises are negligible. After the cancelling of reset KTC noises by CDS, the remaining system noises are mainly the readout circuit noises and the pixel noises dominated by the SF devices.

The sensor is designed with built-in test modes to facilitate the independent characterization of the circuit-only noises and the pixel SF plus circuit noises as shown in Fig. 1(c). In the circuit-only test mode, the switch S1 is turned off and S2 is turned on; an external reference voltage is injected from the terminal TST. In the SF test mode, the switch S1 is turned on and S2 is turned off; the time difference Δt between the double sampling is programmable by register setting. The Δt can be adjusted from 0 μs to 25 μs in 0.1 μs steps. When Δt is zero, the double sampling is correlated with respect to the SF and circuit noises. When Δt is 25 μs, the double sampling with respect to the SF and circuit noises is almost uncorrelated. The main idea of this paper is that, as the Δt is gradually changed from 0 to 25 μs, we could monitor the noises in a transition from the correlated to the uncorrelated double sampling. From the time dependency of this transition, we are able to extract the RTN time constants.

Fig. 2 shows the measured noise histograms for the readout circuit and the pixel SF at $\Delta t = 0$ using the test modes described above. With a 1.34-fF FD capacitance (C_{FD}), the estimated KTC noise at room temperature is about:

$$\frac{1}{q}\sqrt{\frac{k_B T}{C_{FD}}} = 14.6 \text{ e-rms}, \; or, \; \sqrt{k_B T C_{FD}} = 1.75 \text{ mV}, \qquad (1)$$

where k_B is the Boltzmann constant. The measured median noise in Fig. 2 is 0.21 e-rms at 8X gain and 1.72 e-rms at 1X gain. Both are much smaller than the 14.6 e-rms KTC noise. Clearly the KTC noise is effectively canceled by the CDS operation. Furthermore, when Δt is 0, the pixel SF noises are eliminated by the CDS as well, since the measured SF plus circuit noises are almost identical to the circuit-only noises. The nearly parabolic shapes of the noise histograms in Fig. 2 are close to the ideal Gaussian distributions, with only a slight deviation at 8X gain.

III. THE RTN STATISTICAL DISTRIBUTION

Fig. 3 shows the pixel SF plus circuit noises with $\Delta t = 25$ μs, in contrast to those with $\Delta t = 0$ μs. With respect to the SF and circuit noises, the first sampling at $t = 0\mu$s and the second sampling at $t = 25$ μs are essentially uncorrelated.

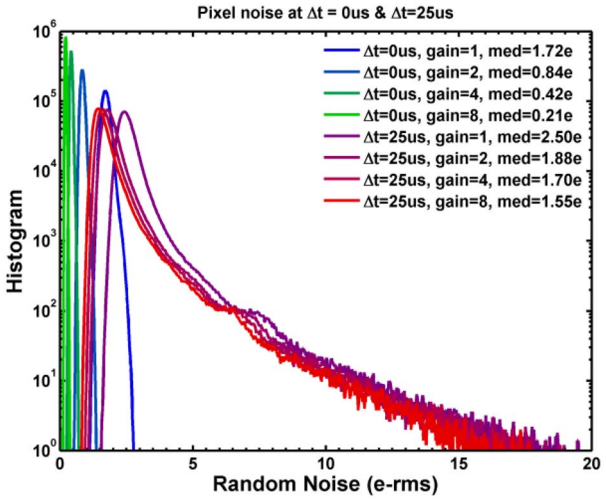

FIGURE 3. **The pixel noises at various gains with $\Delta t = 0$ and $\Delta t = 25\ \mu s$. The histograms change from the tight Gaussian distributions at $\Delta t = 0$ to the ones with significant long tails at $\Delta t = 25\ \mu s$, primarily due to the RTN of the SF devices.**

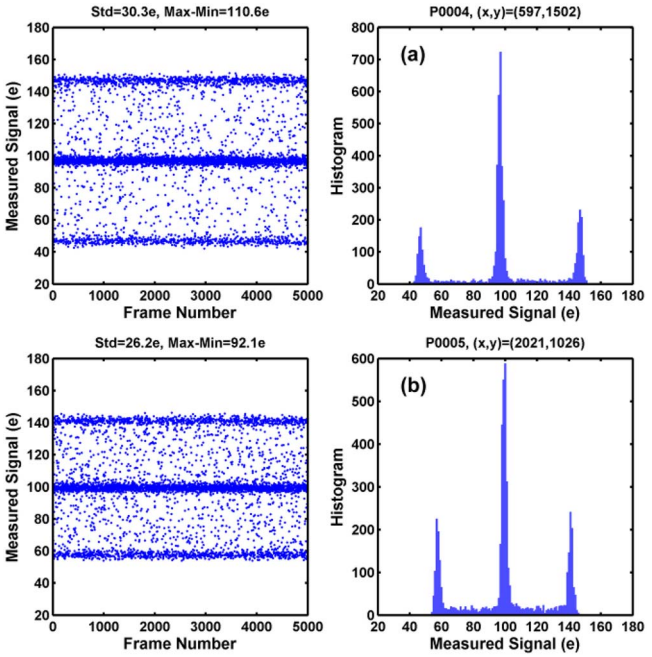

FIGURE 4. **The majority of pixels in the noise distribution tail at $\Delta t = 25\ \mu s$ show clear RTN behavior of discrete signal levels. Two examples are given above. The random telegraph waveforms of 5,000 samples are shown on the left hand side and the signal histograms are on the right hand side.**

The shapes of the histograms change from the tight Gaussian at $\Delta t = 0\ \mu s$ to the distributions with notable long tails on the higher end at $\Delta t = 25\ \mu s$. For the case of 8X gain, the median noise increases from 0.21 e-rms at $\Delta t = 0\ \mu s$ to 1.55 e-rms at $\Delta t = 25\ \mu s$, attributed to both of the SF and the circuit. More importantly, the noise at the extreme end of the tail can be as high as 25 e-rms; or 16 times larger than the median noise.

The gain dependency of the noises helps to distinguish whether the noise sources are down-stream or up-stream from the column amplifiers. The noises near the peaks of histograms show a clear shift towards smaller values as the gain increases, indicating that the sources are mainly in the down-stream circuits from the column amplifiers. They are divided by the gain of the amplifier when input-referred back to the FD node. On the other hand, the long tail portion of the histogram is nearly independent of the gain, suggesting that the sources are up-stream of the amplifier. It means that the noises on the long distribution tail are dominated by the pixel cell SF devices.

The noises of the majority of pixels on the long distribution tail depict the signature RTN waveforms with 3 discrete levels, matching the behavior of a single-trap RTN measured by double sampling [20], [22]. For this reason, the signal and noise distribution tails in the histograms are sometimes referred to as the 'RTN skirts' [21]. Two examples of the pixel RTN waveforms and the corresponding signal histograms are shown in Figs. 4(a) and 4(b). The 3 peaks in the right hand side histograms are well identified. The full width at half maximum (FWHM) of each peak is roughly 3 e- to 4 e-, due to the circuit readout noises. In contrast, the overall RMS noise is 30.3 e-rms in Fig. 4(a) and 26.2 e-rms in Fig. 4(b); much higher than the FWHM of each peak. Evidently the overall noises are dominated by the RTN.

The RTN is generally attributed to the random switching of a single electron trap in a SF NMOS between two discrete levels, corresponding to the occupied and the empty state. Suppose the SF output voltage at the source terminal for the occupied state is higher than that for the empty state by a ΔV. The primary peak represents the case that the trap is in the same state when the double sampling is performed. The upper side peak centered at $+\Delta V$ corresponds to the case that the trap is in the occupied state at the first sampling and in the empty state at the second sampling; vice versa for the lower side peak centered at $-\Delta V$. We found in our samples that about 75% to 85% of the 1,000 noisiest pixels showed 3 well recognized discrete levels.

The central topic of this article is to study and model the single-trap RTN. To highlight the distribution tail where many pixels show clear RTN behaviors, it is customary to plot the inverse cumulative distribution function (ICDF, inverse CDF, or 1 − CDF) of the noise distribution in a semi-log scale as in Fig. 5. The ICDF plot shows that about 99% (ICDF > 0.01) of the pixels have relatively low noises under 5 e-rms; mainly due to the thermal and the flicker noises. Whereas about 0.1% (ICDF < 1E-3) of the pixels in the long tail show noises higher than 8 e-rms with major contribution from the RTN of the pixel SF devices. These top 0.1% pixels are the targets of our investigation.

The ICDF curves in Fig. 5 are approximately straight lines in the high-end region where ICDF is less than 1E-3; similar to the CDF of a Gumbel distribution [37]:

$$-\ln(-\ln(CDF)) = (x-\mu)/\beta, \tag{2}$$

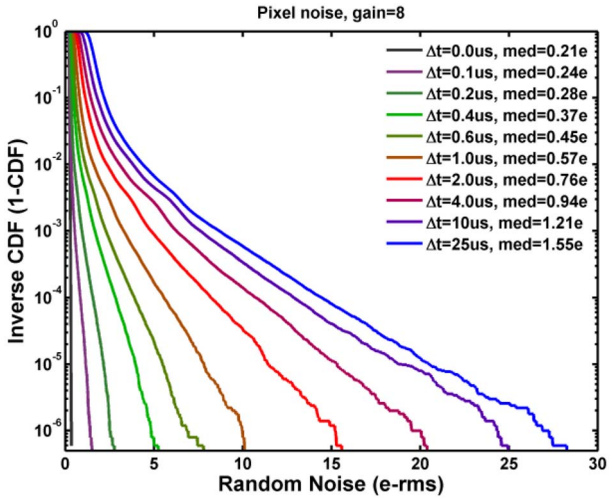

FIGURE 5. **The inverse cumulative distribution functions (ICDF, or 1 − CDF) of the random noises at 8X gain with the double sampling Δt gradually increased from 0μs to 25μs.**

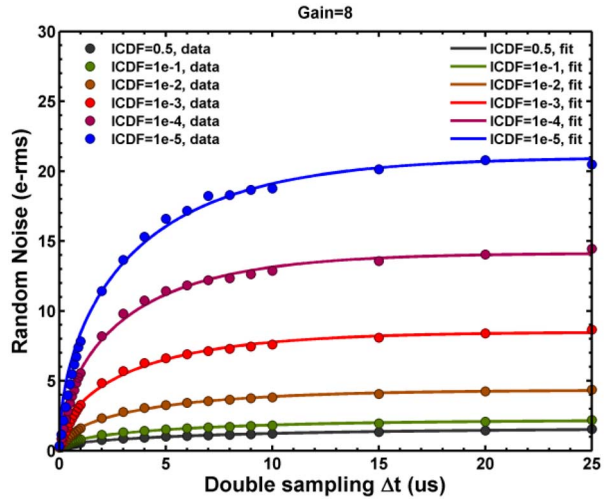

FIGURE 6. **The random noise contours at constant ICDF = 0.5 (the median), 1E-1, 1E-2, 1E-3, 1E-4, and 1E-5 as functions of the double sampling Δt, traced from the curves in Fig. 5, and fit to equation (4) with $\tau_s = 5\mu s$.**

where x is the random noise, μ is the mean, and the standard deviation is $\beta\pi/\sqrt{6}$. The data in Fig. 5 with ICDF = 1 − CDF < 1E-3 show similar linear dependence on x:

$$ln\,(ICDF) \sim ln\,(-ln\,(CDF)) \sim -\,(x-\mu)\,/\beta. \tag{3}$$

From the family of ICDF curves with varying Δt in Fig. 5, we can trace the noise contours at the constant ICDF levels and plot them as functions of Δt. In Fig. 6, six of such curves are plotted for ICDF = 0.5 (the median), 1E-1, 1E-2, 1E-3, 1E-4, and 1E-5, respectively. It appears that the curves follow a similar and well-defined trend of monotonic increasing towards the saturation limits as Δt increases. The data are well fit by the following equation with 2 parameters, the amplitude A and the characteristic time constant τ_s,

$$n_{RTN}\,(t) = A\sqrt{1-e^{-t/\tau_s}}. \tag{4}$$

In the next two Sections, we are going to develop a continuous time model and a discrete event model that lead to above analytical formula. The time constant in Fig. 6 curve fitting is about 5μs. However, the time constants of individual pixels vary from 1 μs to 500 μs, to be discussed in Section VI.

IV. THE CONTINUOUS TIME RTN MODEL

In the continuous-time RTN model for a single-electron trap [1], [17], [18], [22], the trap occupancy probability $P(t)$ can be considered as a smooth function of time. The emission rate $r_e(t)$ and the capture rate $r_c(t)$ of the trap are characterized by the emission and capture time constants, τ_e and τ_c, respectively:

$$r_e\,(t) = \frac{P\,(t)}{\tau_e}; \tag{5}$$

$$r_c\,(t) = \frac{1-P\,(t)}{\tau_c}. \tag{6}$$

Combining the emission and capture processes, the time dependency of the probability function is governed by the first-order differential equation:

$$\frac{dP\,(t)}{dt} = -r_e\,(t) + r_c\,(t) = -\frac{P\,(t)}{\tau_e} + \frac{1-P\,(t)}{\tau_c}. \tag{7}$$

The general solution can be readily expressed as [1]:

$$P\,(t) = \frac{\tau_e}{\tau_e+\tau_c} + \left(P\,(0) - \frac{\tau_e}{\tau_e+\tau_c}\right) e^{-t\left(\frac{1}{\tau_e}+\frac{1}{\tau_c}\right)}. \tag{8}$$

It is clear that the probability function changes exponentially towards a final equilibrium value, regardless of the initial condition:

$$P\,(\infty) = \frac{\tau_e}{\tau_e+\tau_c} (= \text{The probability of occupied}); \tag{9}$$

$$1-P\,(\infty) = \frac{\tau_c}{\tau_e+\tau_c} (= \text{The probability of empty}). \tag{10}$$

The system characteristic time constant τ_s is defined as:

$$\tau_s \overset{\text{def}}{=} \frac{\tau_e\tau_c}{\tau_e+\tau_c}; \text{ or } \frac{1}{\tau_s} = \frac{1}{\tau_c} + \frac{1}{\tau_e}. \tag{11}$$

In the following, the probability function with the initial condition 0 is denoted as $P_0(t)$ and the probability function with the initial condition 1 is denoted as $P_1(t)$:

$$P_0\,(0) = 0; P_0\,(t) = \frac{\tau_e}{\tau_e+\tau_c} - \left(\frac{\tau_e}{\tau_e+\tau_c}\right) e^{-t/\tau_s}; \tag{12}$$

$$P_1\,(0) = 1; P_1\,(t) = \frac{\tau_e}{\tau_e+\tau_c} + \left(\frac{\tau_c}{\tau_e+\tau_c}\right) e^{-t/\tau_s}. \tag{13}$$

The next is to calculate the RTN of such an ideal and simplified trap with binary states measured by the double sampling. Suppose that the first sampling is performed at time 0 and the second sampling is performed at time t. If the trap remains in the same state from time 0 to t, it does not generate any noises. If the trap changes from the occupied state to the empty state by emitting a carrier, a disturbance of

ΔV magnitude is observed in the measured signal. Similarly, if the trap state changes from the empty to the occupied state by capturing a carrier, a $-\Delta$V disturbance is generated in the signal.

The percentage of the RTN traps initially in the empty state is $\tau_c/(\tau_e+\tau_c)$ according to (10) and the percentage of such initially empty traps changing to the occupied states after time t is $(P_0(t)-P_0(0))$ by definition. Similarly, the percentage of the RTN traps initially in the occupied state is $\tau_e/(\tau_e+\tau_c)$ according to (9) and the percentage changing to the empty state after time t is $(P_1(0)-P_1(t))$. Therefore, the total RTN noise power, $n_{RTN}(t)^2$, is simply the weighted sum of the noise power of all the traps either changing from the occupied states to the empty states, or changing from the empty states to the occupied states:

$$n_{RTN}(t)^2 = (\Delta V)^2\left(\frac{\tau_c\,(P_0(t)-P_0(0))}{\tau_e+\tau_c} + \frac{\tau_e\,(P_1(0)-P_1(t))}{\tau_e+\tau_c}\right). \quad (14)$$

Substituting in $(P_0(t)-P_0(0))$ and $(P_1(0)-P_1(t))$ from (12) and (13), the above time-dependent RTN can be rewritten as:

$$n_{RTN}(t) = \frac{\sqrt{2\tau_e\tau_c}}{\tau_e+\tau_c}(\Delta V)\sqrt{1-e^{-t/\tau_s}}. \quad (15)$$

The formula above describes the RTN as a function of the time difference between the first and the second sampling of the double sampling. Note that when the time difference is nearly zero, all traps tend to remain in the same states and the RTN is nearly zero. Consequently, the two samplings are strongly correlated and the RTN is perfectly cancelled by the CDS. As the time difference increases, the correlation is gradually lost. The RTN exponentially increases towards the limiting value. To put it another way, (15) describes the relaxation process from the correlated to the uncorrelated double sampling with a characteristic time constant.

The Fig. 6 in Section III shows that the measured noises at the constant ICDF levels are indeed well matched by the curve fitting using (15). In Section VI we will use (15) further for time constant extraction pixel by pixel.

V. THE DISCRETE EVENT RTN MODEL

Since the RTN is caused by the discrete and random transitions between the empty and the occupied states, it is natural to model it from a discrete event point of view. Because of this discrete nature, the RTN is also historically referred to as the burst noise or the popcorn noise [1]. Similar to the previous section, we will consider a simple and idealized RTN trap with two discrete states. For the convenience of discussion and labeling, we will refer the 2 states as the a-state (occupied) and the b-state (empty). The probabilities of the time periods the trap remaining in the a-state and the b-state are described by the following probability density functions (PDF) [1], [2]:

$$p_a(t) = ae^{-at};\ \int_0^\infty p_a(t)\,dt = 1;\ a \overset{\text{def}}{=} 1/\tau_e; \quad (16)$$

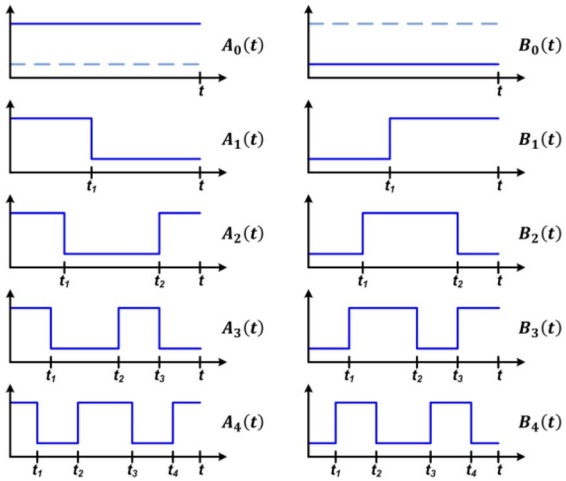

FIGURE 7. The functions $A_n(t)$ and $B_n(t)$ are defined as the probabilities of n transitions during the time interval (0, t) for an ideal RTN trap initially in the a-state and the b-state, respectively.

$$p_b(t) = be^{-bt};\ \int_0^\infty p_b(t)\,dt = 1;\ b \overset{\text{def}}{=} 1/\tau_c. \quad (17)$$

The time constants τ_c and τ_e can be considered as the average time of a trap staying in a-state (t_a) and b-state (t_b):

$$\langle t_a\rangle = \int_0^\infty t p_a(t)\,dt = 1/a = \tau_e; \quad (18)$$

$$\langle t_b\rangle = \int_0^\infty t p_b(t)\,dt = 1/b = \tau_c. \quad (19)$$

In the literature [1], [2], [28]–[35], most of the time constant extraction methods are based on (16) and (17). First, the random telegraph waveform of a DUT is captured with a large number of sample points and the histograms of t_b and t_b distributions are calculated. Then the time constants τ_e and τ_c are extracted from the negative slopes of the histograms in the semi-log plots according to (16) and (17).

As illustrated in Fig. 7, we define a series of functions $A_n(t)$ as the probabilities of exact n transitions happening in the time interval (0, t) if the initial trap states are the a-states, where n is a non-negative integer. Similarly, if the initial states are the b-states, we define the probabilities as the functions $B_n(t)$.

Although there are obvious similarities among (5), (6) and (16), (17), their meanings are interpreted quite differently. The former expresses the changing rates of the probabilities against time (dynamic), while the latter describes the statistical distributions of time periods (static) a trap staying in certain state. The differential equation (7) by itself does not suggest or imply any discrete transitions. It is not intuitively clear how each of the continuous time model and the discrete event model leads to the other on the first sight. The objective of this Section is to establish the link and show that the two models are equivalent.

To begin with, we notice that the trap occupancy probability functions $P_0(t)$ and $P_1(t)$ described in (12) and (13) should be related to the probability functions

$A_n(t)$ and $B_n(t)$ in the following ways according to their corresponding definitions:

$$\sum_{n=0}^{\infty} A_{2n}(t) = P_1(t); \tag{20}$$

$$\sum_{n=0}^{\infty} B_{2n+1}(t) = P_0(t). \tag{21}$$

That is to say, for a trap initially in a-state (occupied), an even number of transitions will bring it back to the same a-state. On the other hand, for a trap initially in b-state (empty), an odd number of transitions are required to bring it to a-state (occupied). Thus, our task is reduced to a mathematical proof of (20) and (21) starting from their respective definitions.

We may calculate the explicit expressions of the functions $A_n(t)$ and $B_n(t)$ from the PDF defined in (16) and (17) in order to carry out the summations in (20) and (21). Starting from the zeroth terms, the functions $A_0(t)$ and $B_0(t)$ represent the probabilities of no transitions in the time interval (0, t). In other words, they are equal to the integrated probabilities of the trap staying in the same state for duration longer than t:

$$A_0(t) = \int_t^{\infty} p_a(t)\,dt = e^{-at}; \tag{22}$$

$$B_0(t) = \int_t^{\infty} p_b(t)\,dt = e^{-bt}. \tag{23}$$

The probability functions of $(n+1)$ transitions are related to the probability functions of n transitions by the following pair of convolution integrations:

$$A_{n+1}(t) = \int_0^t p_a(u)\,B_n(t-u)\,du; \tag{24}$$

$$B_{n+1}(t) = \int_0^t p_b(u)\,A_n(t-u)\,du. \tag{25}$$

In short, the above recursive relations uniquely define the probability functions $A_n(t)$ and $B_n(t)$ to any arbitrary order n. For instance, the explicit expressions for the first five $A_n(t)$ and $B_n(t)$ functions (n = 1 to 5) are given and graphed in the Appendix.

However, it is not convenient to derive a general closed-form expression for an arbitrary n-th term by repetitive integration in the time domain. The only exception is the special case that a equals b, *i.e.*, $\tau_e = \tau_c = \tau$. In this special case, the functions $A_n(t)$ and $B_n(t)$ become identical and the recursive relation leads to the familiar Poisson distribution formula:

$$A_{n+1}(t) = ae^{-at}\int_0^t e^{au}A_n(u)\,du; \tag{26}$$

$$A_n(t) = B_n(t) = \frac{1}{n!}(at)^n e^{-at} = \frac{1}{n!}\left(\frac{t}{\tau}\right)^n e^{-t/\tau}. \tag{27}$$

To deal with the general case of $a \neq b$, the alternative approach is to work on the Laplace transformed counterparts $\bar{A}_n(s)$ and $\bar{B}_n(s)$ in the s-domain. The relations (22), (23), (24), and (25) can be translated into the s-domain as:

$$\bar{A}_0(s) = \frac{1}{s+a}; \tag{28}$$

$$\bar{B}_0(s) = \frac{1}{s+b}; \tag{29}$$

$$\bar{A}_{n+1}(s) = \frac{a}{s+a}\bar{B}_n(s); \tag{30}$$

$$\bar{B}_{n+1}(s) = \frac{b}{s+b}\bar{A}_n(s). \tag{31}$$

Therefore, the explicit expressions for $\bar{A}_n(s)$ and $\bar{B}_n(s)$ are of the forms of the geometric series ($\forall n \geq 0$):

$$\bar{A}_{2n}(s) = \frac{a^n b^n}{(s+a)^{n+1}(s+b)^n}; \tag{32}$$

$$\bar{A}_{2n+1}(s) = \frac{a^{n+1} b^n}{(s+a)^{n+1}(s+b)^{n+1}}; \tag{33}$$

$$\bar{B}_{2n}(s) = \frac{a^n b^n}{(s+a)^n(s+b)^{n+1}}; \tag{34}$$

$$\bar{B}_{2n+1}(s) = \frac{a^n b^{n+1}}{(s+a)^{n+1}(s+b)^{n+1}}. \tag{35}$$

For the special case of $a = b$, the result is simplified to:

$$\bar{A}_n(s) = \bar{B}_n(s) = \frac{a^n}{(s+a)^{n+1}}, \tag{36}$$

which is the Laplace transform of (27) as expected. The completeness relations in the time domain and the s-domain can also be easily verified:

$$\sum_{n=0}^{\infty} \bar{A}_n(s) = \sum_{n=0}^{\infty} \bar{B}_n(s) = \frac{1}{s}, \text{ which implies} \tag{37}$$

$$\sum_{n=0}^{\infty} A_n(t) = \sum_{n=0}^{\infty} B_n(t) = 1. \tag{38}$$

The required summation over all the even and odd terms in (20) and (21) can be calculated straightforwardly:

$$\overline{P_1}(s) = \sum_{n=0}^{\infty} \bar{A}_{2n}(s) = \frac{s+b}{s(s+a+b)}; \tag{39}$$

$$\overline{P_0}(s) = \sum_{n=0}^{\infty} \bar{B}_{2n+1}(s) = \frac{b}{s(s+a+b)}. \tag{40}$$

Finally, performing the inverse Laplace transforms on above equations we get the following time-domain counterparts:

$$P_1(t) = \sum_{n=0}^{\infty} A_{2n}(t) = \frac{b}{a+b} + \frac{a}{a+b}e^{-(a+b)t}; \tag{41}$$

$$P_0(t) = \sum_{n=0}^{\infty} B_{2n+1}(t) = \frac{b}{a+b} - \frac{b}{a+b}e^{-(a+b)t}. \tag{42}$$

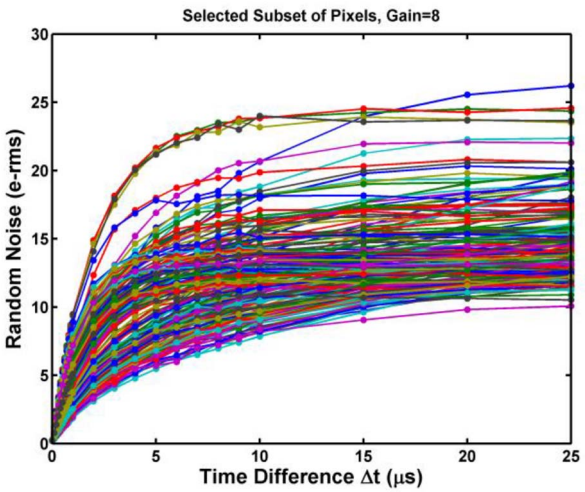

FIGURE 8. **The random noise as a function of the double sampling time difference Δt for 200 selected pixels in the region of ICDF < 1E-3.**

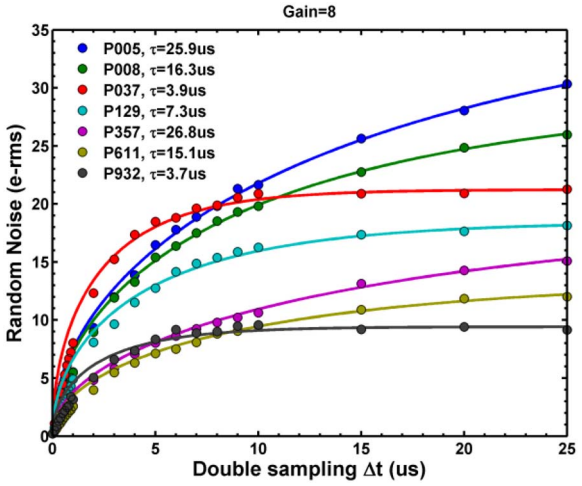

FIGURE 9. **A selected set of 7 pixels from the top 1,000 pixels showing a variety of characteristic time constants extracted by curve fitting to (15).**

The above results are exactly the same as (12) and (13) when the parameters a and b are replaced by $1/\tau_e$ and $1/\tau_c$, respectively. Accordingly, we get the same RTN equation (15) following the calculation in (14).

In quick summary, we started with two seemingly different approaches, the continuous time differential equation approach and the discrete event probability approach, and we showed that the latter lead to the identical result derived by the former. To be specific, we formally proved the equivalence of these two models. The explicit closed-form expressions for the individual functions $A_n(t)$ and $B_n(t)$ can be obtained by the inverse Laplace transform of (32), (33), (34), and (35) as well; the results are given in the Appendix.

VI. PIXEL BY PIXEL TIME CONSTANT EXTRACTION

Having established the validity of the RTN equation (15), we now proceed to extract the characteristic time constants for individual pixels by nonlinear curve fitting. As discussed in Section III and shown in Fig. 2, about 99% of the pixels have relatively low noises. It is very likely they do not have traps showing clear RTN behaviors; or the small RTN is mixed indistinguishably with the background thermal noises and flicker noises. On the other hand, the pixels in the long tail portion of the noise histograms or the ICDF curves, accounting for 0.1% or less of the total population, have larger noises and higher tendency to show clear RTN characteristics. As such, we direct our attention to the noisiest 1,000 pixels of the 8.3 Mpixel array in the region of ICDF < 1E-3 at $\Delta t = 25\ \mu s$ and perform the time constant extraction pixel by pixel.

Fig. 8 shows the RTN time dependency of a subset of 200 pixels with various time constants and noise amplitudes. Fig. 9 shows the representative curve fitting results for 7 selected pixels, each labeled by the extracted time constants. All data set are reasonably well fit by the analytical formula (15). Figs. 10(a) and 10(b) summarize the statistical

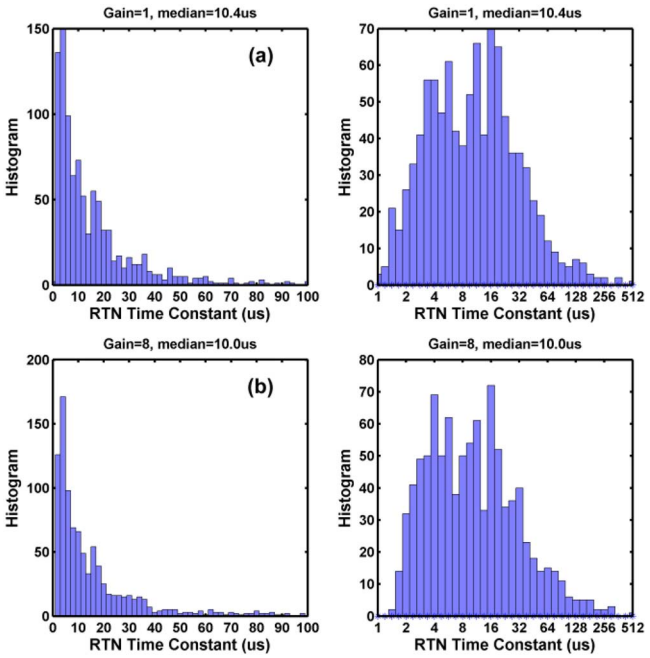

FIGURE 10. **The distributions of the extracted characteristic time constants at 1X gain in (a), and 8X gain in (b). The histograms are calculated for linearly spaced bins (left) and the logarithmically spaced bins (right) separately.**

distributions of the extracted time constants of 1,000 pixels at 1X and 8X gains, respectively. The histograms are plotted with both linearly spaced bins on the left hand side and the logarithmically spaced bins on the right hand side. We observe that the majority of the time constants fall into the range of 1 μs to 500 μs, with relatively few numbers scattered beyond 500 μs. The median time constant is about 10 μs. Interestingly, the overall noise distribution when all pixels are included shows an averaged behavior corresponding to a time constant of 5 μs as in Fig. 6.

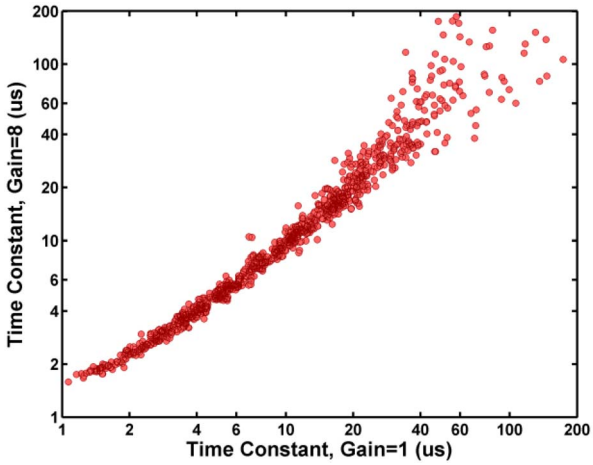

FIGURE 11. **The correlation between the time constants extracted at 8X gain and those extracted at 1X gain. A discrepancy at the low end is due the circuit setting time difference. At 1X gain, the circuit settling time is about 0.24μs, while at 8X gain the settling time is about 0.64μs.**

It is important to point out that the ideal RTN time dependent equation (15) does not take into account the readout circuit setting time. In this CIS chip, the settling time of the front-end column amplifier is affected by the capacitance ratio of C1 and C2. At 8X gain, the downstream circuit noises are reduced by a factor of 8; therefore, the measured pixel noises are more accurate. However, at 8X gain, the circuit settling time constant is increased by the larger feedback factor of C1/C2. The simulated circuit settling time constant is about 0.24 μs at 1X gain and 0.64 μs at 8X gain. As a result, we expect that the time constants less than 3 μs extracted from data of 8X gain would be slightly higher than those extracted from the data measured at 1X gain, as reflected in the correlation plot in Fig. 11. A more detailed study on how the circuit settling time affects the RTN time constant extraction quantitatively is still in progress and will be reported elsewhere.

In the current chip design and measurement setup, the programmable double sampling time difference has an upper bound of 25 μs. The RTN time constants much longer than 25 μs would be extracted less accurately comparing to the shorter time constants due to the insufficient range of time for curve fitting. This explains why the data points in Fig. 11 are more tightly correlated on the lower side of the plot and are more scattered on the higher side. Roughly 4% of the extracted time constants are larger than 500 μs. They cannot be determined precisely, since (4) becomes degenerated when $t/\tau_s \ll 1$:

$$n_{RTN}(t) \sim A\sqrt{t/\tau_s}. \tag{43}$$

Similar to other reports [20], [22], we also observe that the pixel noise behaviors are very much diversified even among the top 1,000 pixels. We find that about 75% to 85% of the 1,000 pixels show 3 peaks distinctively in the waveforms and the histograms of the sampled signals. Some of them show more clean-cut and concentrated populations around

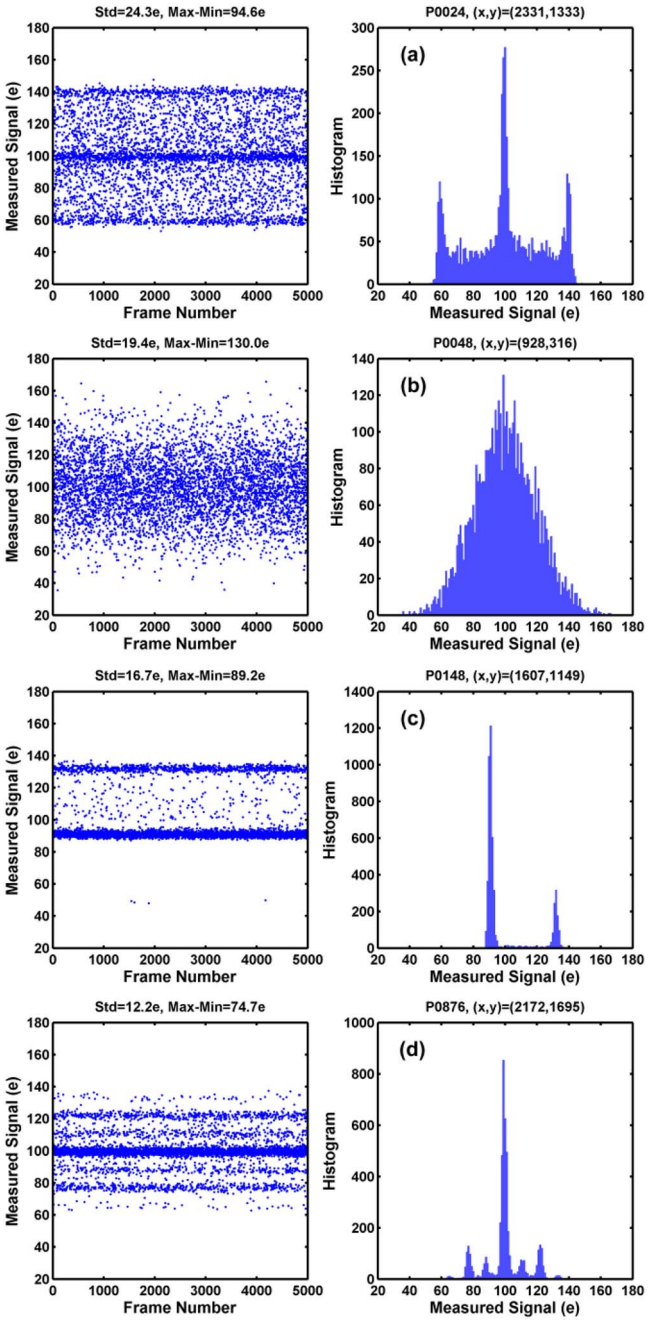

FIGURE 12. **A variety of noise distributions and behaviors are observed among the top 1,000 pixels. (a) About 75% to 85% of the pixels show 3 peaks; (b) about 6% to 16% of the pixels show one broad peak; (c) about 8% of the pixels show 2 peaks; and (d) about 1% of the pixels show more than 3 peaks.**

the 3 peaks such as the examples in Figs. 4(a) and 4(b). But some other pixels with 3 peaks show large numbers of data points located between the main peak and the two side peaks, as shown in Fig. 12(a). The intermediate data points are in general due to the inadequate circuit settling [20]. About 6% to 16% of the pixels show only one broad peak as in Fig. 12(b). About 8% of the pixels show 2 asymmetric peaks as in Fig. 12(c). The natures of these 2 types of behaviors are not well understood and are still under study.

Some of the pixels with very short time constants show 3 peaks under 1X gain, but only 1 peak under 8X gain; apparently due to the circuit settling limitation. About 1% of the pixels show more than 3 peaks as in Fig. 12(d), suggesting the existence or more than one trap. It is typically assumed that the number of traps per device n follows the Poisson distribution [38], [39]:

$$f(n) = \frac{1}{n!}\lambda^n e^{-\lambda}, \tag{44}$$

where λ is the average number of traps per device. For a small λ, we get the following approximations:

$$f(0) \sim 1 - \lambda + \frac{1}{2}\lambda^2; f(1) \sim \lambda - \lambda^2; f(2) \sim \frac{1}{2}\lambda^2; \lambda \ll 1. \tag{45}$$

In our test chips, the probability of 1 trap, $f(1)$, is estimated to be roughly between 1% and 0.1%, and the probability ratio of 2 traps versus 1 trap, $f(2)/f(1)$, is in the order of 1%. In comparison, these seem to be much smaller than the numbers reported in [33], [34], [38], and [39], likely due to the differences in device designs, sizes, bias conditions, and the fabrication processes. We plan to examine a much larger sample size to check out the validity of (44).

The RTN equation (15) is derived for the ideal single-trap behaviors such as the representative model pixels shown in Figs. 4(a) and 4(b). Nevertheless, the time dependency of the random noises can be fit well by (15) regardless the variety of distribution shapes. For the non-ideal cases, the extracted time constants may be simply considered as the empirical parameters describing the experimental data. The understanding and modeling of the diversity of the noise behavior is outside the scope of this study.

VII. CONCLUSION

Most of the RTN time constant extraction reported in the literature was based on the measured telegraphic waveforms from the stand-alone test key device or an array of devices. In this paper we presented an additional method suitable for CIS on-chip time constant extraction. This is potentially useful for CIS products with the similar double sampling circuits, CIS process development, and yield enhancement engineering.

The key equation describing the RTN dependence on the double sampling time difference (15) is derived theoretically from two models, the continuous time model in Section IV and the discrete event model in Section V.

In this study we only discussed the extraction of the RTN characteristic time constant, $\tau_s = \tau_e\tau_c/(\tau_e+\tau_c)$. Further work is required to obtain the emission and capture time constants separately. The extracted time constants from our data mostly fall into the range between 1 μs and 500 μs. The accuracy of the extraction is limited by the circuit settling time at the lower end, and the insufficient range of curve fitting on the higher end. In comparison, the data in [33] showed a much wider range of RTN time constants up to 6 orders of magnitude, from 5 μs to 1 s, under various bias conditions. The RTN parameters are known to be highly sensitive to the technology nodes and the fabrication process details. These will be the area for future investigation.

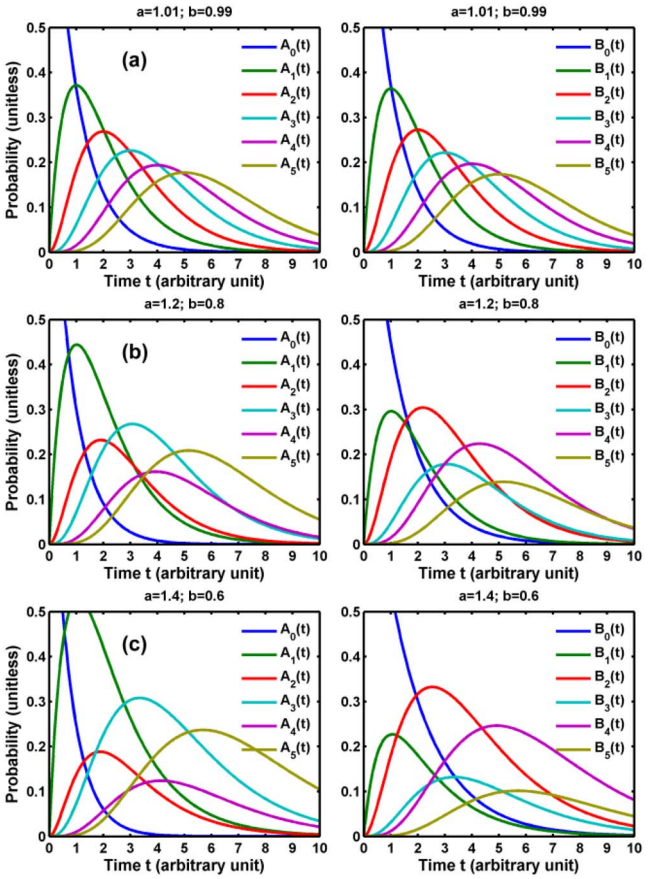

FIGURE 13. Examples of the discrete event probability functions $A_n(t)$ and $B_n(t)$ defined in Fig. 7, and expressed in (46)-(51). From top to bottom, $(a, b) = (1.01, 0.99)$, $(1.2, 0.8)$, and $(1.4, 0.6)$.

APPENDIX

The first five terms of the functions $A_n(t)$ and $B_n(t)$ can be obtained from (22) and (23) by carrying out the recursive integrations in (24) and (25) directly as follows, where $z \overset{\text{def}}{=} (a-b)t$ for simplification:

$$A_1(t) = \frac{a}{a-b}\left(-e^{-at} + e^{-bt}\right); \tag{46}$$

$$A_2(t) = \frac{ab}{(a-b)^2}\left(-(1+(a-b)t)\,e^{-at} + e^{-bt}\right); \tag{47}$$

$$A_3(t) = \frac{a^2b}{(a-b)^3}\left((2+z)\,e^{-at} - (2-z)\,e^{-bt}\right); \tag{48}$$

$$A_4(t) = \frac{a^2b^2}{(a-b)^4}\left(\left(3+2z+\frac{1}{2}z^2\right)e^{-at} - (3-z)\,e^{-bt}\right); \tag{49}$$

$$A_5(t) = \frac{a^3b^2}{(a-b)^5}\left(\left(-6-3z-\frac{z^2}{2}\right)e^{-at} + \left(6-3z+\frac{z^2}{2}\right)e^{-bt}\right). \tag{50}$$

The companion functions $B_n(t)$ are related to the functions $A_n(t)$ by the symmetry relation below, as implied by (22), (23), (24), and (25):

$$B_n(t, a, b) = A_n(t, b, a), \forall n. \tag{51}$$

The time dependencies of the functions are plotted in Fig. 13 for 3 examples of (a, b). When a and b are approximately equal, both of $A_n(t)$ and $B_n(t)$ functions approach the Poisson distribution (27).

The closed-form time-domain probability functions can be obtained by the inverse Laplace transform of (32) and (33) using the standard partial-fraction expansion techniques [40]:

$$\bar{A}_{2n}(s) = \frac{a^n b^n}{(a-b)^{2n}} \left(\sum_{k=1}^{n+1} \frac{(-1)^n (2n-k)!}{(n-1)!(n+1-k)!} \frac{(a-b)^{k-1}}{(s+a)^k} + \sum_{k=1}^{n} \frac{(-1)^{n+k} (2n-k)!}{n!(n-k)!} \frac{(a-b)^{k-1}}{(s+b)^k} \right); \tag{52}$$

$$\bar{A}_{2n+1}(s) = \frac{a^{n+1} b^n}{(a-b)^{2n+1}} \left(\sum_{k=1}^{n+1} \frac{(-1)^{n+1} (2n+1-k)!}{n!(n+1-k)!} \frac{(a-b)^{k-1}}{(s+a)^k} + \sum_{k=1}^{n+1} \frac{(-1)^{n+1+k} (2n+1-k)!}{n!(n+1-k)!} \frac{(a-b)^{k-1}}{(s+b)^k} \right); \tag{53}$$

$$A_{2n}(t) = \frac{a^n b^n}{(a-b)^{2n}} \left(\left(\sum_{k=1}^{n+1} \frac{(-1)^n (2n-k)! ((a-b)t)^{k-1}}{(n-1)!(n+1-k)!(k-1)!} \right) e^{-at} + \left(\sum_{k=1}^{n} \frac{(-1)^{n+k} (2n-k)! ((a-b)t)^{k-1}}{n!(n-k)!(k-1)!} \right) e^{-bt} \right); \tag{54}$$

$$A_{2n+1}(t) = \frac{a^{n+1} b^n}{(a-b)^{2n+1}} \left(\left(\sum_{k=1}^{n+1} \frac{(-1)^{n+1} (2n+1-k)! ((a-b)t)^{k-1}}{n!(n+1-k)!(k-1)!} \right) e^{-at} + \left(\sum_{k=1}^{n+1} \frac{(-1)^{n+1+k} (2n+1-k)! ((a-b)t)^{k-1}}{n!(n+1-k)!(k-1)!} \right) e^{-bt} \right). \tag{55}$$

REFERENCES

[1] M. J. Kirton and M. J. Uren, "Noise in solid-state microstructures: A new perspective on individual defects, interface states and low-frequency (1/*f*) noise," *Adv. Phys.*, vol. 38, no. 4, pp. 367–468, 1989.

[2] K. K. Hung, P. K. Ko, C. Hu, and Y. C. Cheng, "An automated system for measurement of random telegraph noise in metal-oxide-semiconductor field-effect transistors," *IEEE Trans. Electron Devices*, vol. 36, no. 6, pp. 1217–1219, Jun. 1989.

[3] Z. Shi, J.-P. Mieville, and M. Dutoit, "Random telegraph signals in deep submicron n-MOSFET's," *IEEE Trans. Electron Devices*, vol. 41, no. 7, pp. 1161–1168, Jul. 1994.

[4] G. Ghibaudo and T. Boutchacha, "Electrical noise and RTS fluctuations in advanced CMOS devices," *Microelectron. Rel.*, vol. 42, nos. 4–5, pp. 573–582, 2002.

[5] E. Simoen and C. Claeys, "Random telegraph signal: A local probe for single point defect studies in solid-state devices," *Mater. Sci. Eng. B*, vols. 91–92, pp. 136–143, Apr. 2002.

[6] E. Simoen, B. Kaczer, M. Toledano-Luque, and C. Claeys, "Random telegraph noise: From a device physicist's dream to a designer's nightmare," *Electrochem. Soc. Trans.*, vol. 39, no. 1, pp. 3–15, 2011.

[7] K. Walczak and T. L. Reinecke, "Scaling rules for telegraph noise," *IEEE Trans. Nanotechnol.*, vol. 10, no. 6, pp. 1224–1230, Nov. 2011.

[8] Y. Mori, K. Ohyu, K. Okonogi, and R.-I. Yamada, "The origin of variable retention time in DRAM," in *Proc. IEEE Int. Electron Devices Meeting*, Washington, DC, USA, Dec. 2005, pp. 1034–1037.

[9] B. Oh *et al.*, "Characterization of an oxide trap leading to random telegraph noise in gate-induced drain leakage current of DRAM cell transistors," *IEEE Trans. Electron Devices*, vol. 58, no. 6, pp. 1741–1747, Jun. 2011.

[10] K. Takeuchi, T. Nagumo, and T. Hase, "Comprehensive SRAM design methodology for RTN reliability," in *Proc. Symp. VLSI Circuits*, Honolulu, HI, USA, Jun. 2011, pp. 130–131.

[11] S. O. Toh, T.-J. K. Liu, and B. Nikoliæ, "Impact of random telegraph signaling noise on SRAM stability," in *Proc. Symp. VLSI Technol.*, Honolulu, HI, USA, Jun. 2011, pp. 204–205.

[12] H. Miki *et al.*, "Quantitative analysis of random telegraph signals as fluctuations of threshold voltages in scaled flash memory cells," in *Proc. 45th Int. Rel. Phys. Symp.*, Phoenix, AZ, USA, Apr. 2007, pp. 29–35.

[13] D. Kang *et al.*, "A new approach of NAND flash cell trap analysis using RTN characteristics," in *Proc. Symp. VLSI Technol.*, Honolulu, HI, USA, Jun. 2011, pp. 206–207.

[14] T. Matsumoto, K. Kobayashi, and H. Onodera, "Impact of random telegraph noise on CMOS logic delay uncertainty under low voltage operation," in *Proc. IEEE Int. Electron Devices Meeting*, San Francisco, CA, USA, Dec. 2012, pp. 25.6.1–25.6.4.

[15] M. Luo *et al.*, "Impacts of random telegraph noise (RTN) on digital circuits," *IEEE Trans. Electron Devices*, vol. 62, no. 6, pp. 1725–1732, Jun. 2015.

[16] K. M. Findlater *et al.*, "Source follower noise limitations in CMOS active pixel sensors," in *Proc. SPIE Detectors Assoc. Signal Process.*, vol. 5251. Saint-Étienne, France, pp. 187–195, 2004, doi: 10.1117/12.512969.

[17] J. S. Kolhatkar *et al.*, "Modeling of RTS noise in MOSFETs under steady-state and large-signal excitation," in *Proc. IEEE Int. Electron Devices Meeting*, San Francisco, CA, USA, Dec. 2004, pp. 759–762.

[18] E. Hoekstra, "Large signal excitation measurement techniques for RTS noise in MOSFETs," in *Proc. EUROCON*, Belgrade, Serbia, Nov. 2005, pp. 1863–1866.

[19] C. Leyris *et al.*, "Response of correlated double sampling CMOS imager circuit to random telegraph signal noise," in *Proc. IEEE Int. Caribbean Conf. Devices Circuits Syst.*, Playa del Carmen, Mexico, Apr. 2006, pp. 109–114.

[20] J. Janesick, J. T. Andrews, and T. Elliott, "Fundamental performance differences between CMOS and CCD imagers: Part I," in *Proc. SPIE High Energy Opt. Infrared Detectors Astron. II*, vol. 6276. Orlando, FL, USA, 2006, Art. no. 62760M, doi: 10.1117/12.678867.

[21] J. Janesick *et al.*, "Fundamental performance differences between CMOS and CCD imagers: Part IV," in *Proc. SPIE High Energy Opt. Infrared Detectors Astron. IV*, vol. 7742. San Diego, CA, USA, 2010, Art. no. 77420B, doi: 10.1117/12.862491.

[22] X. Wang, P. R. Rao, A. Mierop, and A. J. P. Theuwissen, "Random telegraph signal in CIS pixels," in *Proc. IEEE Int. Electron Devices Meeting*, San Francisco, CA, USA, Dec. 2006, pp. 115–118.

[23] X. Wang, M. F. Snoeij, P. R. Rao, A. Mierop, and A. J. P. Theuwissen, "A CMOS image sensor with a buried-channel source follower," in *Proc. Int. Solid State Circuits Conf.*, San Francisco, CA, USA, Feb. 2008, pp. 62–63.

[24] Y. Chen, X. Wang, A. J. Mierop, and A. J. P. Theuwissen, "A CMOS image sensor with in-pixel buried-channel source follower and optimized row selector," *IEEE Trans. Electron Devices*, vol. 56, no. 11, pp. 2390–2397, Nov. 2009.

[25] P. Martin-Gonthier and P. Magnan, "Low-frequency noise impact on CMOS Image sensors," in *Proc. 24th Conf. Design Circuits Integr. Syst.*, Zaragoza, Spain, Nov. 2009, pp. 18–20.

[26] P. Martin-Gonthier and P. Magnan, "RTS noise impact in CMOS image sensors readout circuit," in *Proc. 16th Int. Conf. Electron. Circuits Syst.*, Hammamet, Tunisia, Dec. 2009, pp. 928–931.

[27] P. Martin-Gonthier, E. Havard, and P. Magnan, "Custom transistor layout design techniques for random telegraph signal noise reduction in CIS," *IEEE Electron. Lett.*, vol. 46, no. 19, pp. 1323–1324, Sep. 2010.

[28] K. Abe *et al.*, "Analysis of source follower random telegraph signal using nMOS and pMOS array TEG," in *Proc. Int. Image Sensor Workshop*, Ogunquit, ME, USA, Jun. 2007, pp. 62–65.

[29] T. Fujisawa *et al.*, "Analysis of hundreds of time constant ratios and amplitudes of random telegraph signal with very large scale array test pattern," *Jpn. J. Appl. Phys.*, vo1. 49, no. 4S, pp. 1–4, 2010.
[30] K. Abe *et al.*, "Experimental investigation of effect of channel doping concentration on random telegraph signal noise," *Jpn. J. Appl. Phys.*, vol. 49, no. 4S, 2010, Art. no. 04DC07.
[31] A. Yonezawa *et al.*, "Statistical analysis of random telegraph noise reduction effect by separating channel from the interface," in *Proc. Int. Rel. Phys. Symp.*, Anaheim, CA, USA, Apr. 2012, pp. 3B.5.1–3B.5.7.
[32] R. Kuroda *et al.*, "A statistical evaluation of random telegraph noise of in-pixel source follower equivalent surface and buried channel transistors," *IEEE Trans. Electron Devices*, vo1. 60, no. 10, pp. 3555–3561, Oct. 2013.
[33] T. Obara *et al.*, "Extraction of time constants ratio over nine orders of magnitude for understanding random telegraph noise in MOSFETs," *Jpn. J. Appl. Phys.*, vo1. 53, no. 4S, 2014, Art. no. 04ECI9.
[34] T. Obara *et al.*, "Analyzing correlation between multiple traps in RTN characteristics," in *Proc. Int. Rel. Phys. Symp.*, Jun. 2014, pp. 4A.6.1–4A.6.7.
[35] R. Kuroda, A. Teramoto, and S. Sugawa, "Random telegraph noise measurement and analysis based on arrayed test circuit toward high S/N CMOS image sensors," in *Proc. 29th Int. Conf. Microelectron. Test Struct.*, Yokohama, Japan, Mar. 2016, pp. 46–51.
[36] J. R. Janesick, *Photon Transfer: DN* $\rightarrow \lambda$ (SPIE Press, PM 170). Bellingham, WA, USA: SPIE, 2007, chs. 4–5, pp. 35–78.
[37] C. Walck, "Hand-book on statistical distributions for experimentalists," Particle Phys. Group, Dept. Phys., Univ. Stockholm, Stockholm, Sweden, Tech. Rep. SUF-PFY/96-01, 2007.
[38] S. Realov and K. L. Shepard, "Random telegraph noise in 45-nm CMOS: Analysis using an on-chip test and measurement system," in *Proc. IEEE Int. Electron Devices Meeting*, San Francisco, CA, USA, Dec. 2010, pp. 28.2.1–28.2.4.
[39] S. Realov and K. L. Shepard, "Analysis of random telegraph noise in 45-nm CMOS using on-chip characterization system," *IEEE Trans. Electron Devices*, vo1. 60, no. 5, pp. 1716–1722, May 2013.
[40] J. L. Schiff, *The Laplace Transform: Theory and Applications*. New York, NY, USA: Springer-Verlag, 1999, ch. 1, sec. 1.10, pp. 35–39.

CALVIN YI-PING CHAO received the M.S. and Ph.D. degrees in electrical and computer engineering from the University of Illinois at Urbana–Champaign, IL, USA, in 1987 and 1992, respectively. He was with MicroMedia Inc., e-Phocus Inc., Burr-Brown Corporation, and IBM Microelectronics, on diverse projects including CIS design, image processing, analog and mixed-signal IC design, device modeling, characterization, reliability physics, and process development. He is currently the Deputy Director of Mixed Signal and RF Solution Division, Research and Development, Taiwan Semiconductor Manufacturing Company. He has authored 25 papers and holds 26 U.S. patents.

HONYIH TU received the B.S. degree in electrical engineering from National Central University, Zhongli, Taiwan, in 1993. From 1995 to 2005, he was a Designer, a Project Leader, and a Product Manager for digital still cameras. From 2006 to 2009, he engaged in CIS ISP development, turnkey solutions, and customer support. He joined Taiwan Semiconductor Manufacturing Company in 2010, where he is responsible for system software and hardware integration for CIS characterization. His interests include image sensor applications, imaging systems, and ISP algorithm development.

THOMAS WU received the B.S. and M.S. degrees in engineering science from National Cheng Kung University, Tainan, Taiwan, in 2000 and 2003, respectively. From 2004 to 2008, he was an Assistant Researcher with the Instrument Technology Research Center, National Applied Research Laboratories, Hsinchu, Taiwan. In 2014, he joined Taiwan Semiconductor Manufacturing Company. His research interests include CMOS image sensor characterization, applications, and systems.

KUO-YU CHOU received the B.S. and M.S. degrees in communication engineering from National Chiao Tung University, Hsinchu, Taiwan, in 1996 and 1998, respectively. He is specialized in high speed ADC, low noise circuit, and CMOS image sensor designs. He is currently a Design Manager of the CIS Design Program in Taiwan Semiconductor Manufacturing Company.

SHANG-FU YEH received the B.S. and M.S. degrees in electrical engineering from National Central University, Zhongli, Taiwan, in 2001 and 2003, respectively, and the Ph.D. degree in electrical engineering from National Tsing-Hua University, Hsinchu, Taiwan, in 2014. From 2003 to 2008, he designed IO, low dropout regulators, and high speed interface circuits with EE-Solutions Inc., Hsinchu. In 2012, he joined the Taiwan Semiconductor Manufacturing Company, where he is currently a Mixed-Signal Circuit Designer. His research interests include low noise and high speed CMOS image sensors design.

FU-LUNG HSUEH received the Ph.D. degree in electrical engineering from Lehigh University in 1982. In 1981, he was with RCA David Sarnoff Research Center, Princeton, NJ, USA, for 22 years. He joined Taiwan Semiconductor Manufacturing Company in 2003, where he is a TSMC Academy Fellow and the Director of Mixed-Signal and RF Solution Division, Research and Development. He has 93 patents issued and over 77 papers published. His expertise includes very large scale integration (VLSI) circuit design, high-speed ADCs, DACs, RF building blocks (LNA, VCO, synthesizers), CMOS image sensors, CCDs, high-speed interfaces, advanced PLL frequency synthesizers, high density active-matrix electroluminescent display (AMEL) in SOI, infrared PtSi imagers, single-event upset immune, and state-retention memories.

He was a recipient of Five Technical Achievement Awards in 2002, 1997, 1994, 1992, 1989, respectively, at Sarnoff Corporation, three TSMC Chairman Innovation Awards, in 2007 and 2008, and Two Best Paper Awards from SOI and SID Conferences in 1994. He was an ISSCC TPC member in Technology Directions from 2011 to 2015, as the Session Chair and the Co-Chair, and as a Tutorial and a Forum Coordinators from 2014 to 2015. He gave a short course at 2012 Symposium on VLSI Circuits, Hawaii, and served as a Panelist of an evening Rump session at 2013 Symposium on VLSI Circuits, Kyoto, Japan. He was a TPC Member of A-SSCC from 2008 to 2011.